Highly reversible oxygen redox chemistry of Li_2RuO_3 enabled by a stabilizing electrode-electrolyte interphase with sulfide solid electrolyte

Yuqi Wu, Ke Zhou, Fucheng Ren, Yang Ha, Ziteng Liang, Xuefan Zheng, Zhengyu Wang, Wu Yang, Maojie Zhang, Mingzeng Luo, Corsin Battaglia, Wanli Yang, Lingyun Zhu, Zhengliang Gong and Yong Yang**

Y. Q. Wu and K. Zhou contributed equally to this work.

Y. Q. Wu, F. C. Ren, X. F. Zheng, W. Yang, Prof. Z. L. Gong
School of Energy, Xiamen University, Xiamen 361005, China
E-mail: (zlgong@xmu.edu.cn, yyang@xmu.edu.cn)

K. Zhou, Z. T. Liang, M. J. Zhang, M. Z. Luo, Prof. Y. Yang
State Key Laboratory for Physical Chemistry of Solid Surfaces, and Department of Chemistry, College of Chemistry and Chemical Engineering, Xiamen University, Xiamen 361005, China

K. Zhou, Dr. Corsin Battaglia
Empa, Swiss Federal Laboratories for Materials Science and Technology, 8600 Dübendorf, Switzerland

Dr. Y. Ha, Prof. W. L. Yang
Advanced Light Source, Lawrence Berkeley National Laboratory, Berkeley, CA 94720, USA

Z.Y. Wang, Prof. L. Y. Zhu
Guilin Electrical Equipment Scientific Research Institute Co., Ltd, Guilin 541004, China

Keywords: All solid-state batteries, Lithium-rich material, Li_2RuO_3, Reversible oxygen redox, Passivating electrode-electrolyte interphases

Abstract

The practical application of high-capacity lithium-rich cathode materials in lithium-ion batteries has been largely restricted by severe side reactions with electrolytes. Herein, we enable the stable cycling of an uncoated lithium-rich Li_2RuO_3 cathode by forming a passivating solid electrolyte interphase at the interface with a sulfide solid electrolyte for all-solid-state lithium batteries (ASSLBs), which suppresses serious parasitic interfacial reactions and fast-increasing interfacial impedance observed in liquid electrolytes. The exceptionally high interfacial stability of the Li_2RuO_3/sulfide electrolyte interface contributes to a high reversible capacity of 257 mAh g^{-1} at 0.05 C, and unprecedented cycling stability with 90% capacity retention after 1000 cycles at 1 C. Experimental characterization and first-principles calculations demonstrate that electronically insulating interfacial reaction products forming at the interface between the Li_2RuO_3 cathode and the sulfide electrolyte facilitate the formation of a stable and passivating interphase. Importantly, reversible oxygen redox activity is well-maintained in Li_2RuO_3 ASSLBs even after 600 cycles, and the voltage decay is significantly reduced. These new discoveries demonstrate the critical role of interface design for achieving prolonged cycling stability of lithium-rich cathode materials.

1. Introduction

With the rapid development of electric vehicles and grid energy storage, traditional cathode materials cannot fully meet market demand for high-energy-density lithium-ion batteries, such as $LiNi_{1-x-y}Mn_xCo_yO_2$ (practical capacity about 200 mAh g^{-1}), $LiFePO_4$ (140 mAh g^{-1}), etc.[1] Lithium-rich layered oxides have successfully attracted significant attentions as promising high-capacity cathode materials due to their high capacity over 250 mAh g^{-1} based on the active anionic (oxygen) redox on top of the cationic redox.[2] However, the commercialization of lithium-rich layered cathodes is still restricted due to various problems, such as poor cycling stability, undesirable rate capability, and large voltage decay during repeated cycling in cells with liquid electrolytes (LIBs).[3]

Therefore, tremendous efforts have been carried out to find the origin of these issues. It was found that the unstable electrode/electrolyte interphase and continuous parasitic interfacial reactions upon cycling played a key role in capacity loss and voltage decay.[1b, 4] In order to activate the oxygen redox of lithium-rich layered materials, the charging cut-off potential is relatively high (more than 4.3 V vs Li/Li^+) and outside the electrochemical voltage stability window of typical liquid organic electrolytes, resulting in continuous oxidative decomposition.[4c, 5] Moreover, the deeply delithiated cathodes themselves are also chemically unstable, forming a thick cathode electrolyte interphase (CEI) layer with the liquid electrolyte.[6] Besides, acidification of the electrolyte during the cycling process due to the formation of hydrofluoric acid leads to transition metal dissolution and corrosion from the cathode particle surface, accelerating structural degradation and leading to voltage and capacity decay.[4a] In particular, the continuous oxygen loss during cycling is closely related to the unstable electrode/electrolyte interface. Many researches have shown oxygen loss in the form of gas released from the lattice of the material resulting in the formation vacancies and pores in the particles.[7] In addition, oxygen diffusion pathways nearby these pores, which will proliferate and extend during cycles in the LIBs, accelerating the structural degradation, further oxygen loss, and voltage fade.[1b]

To solve the interfacial problems of lithium-rich layered materials with liquid electrolytes, the use of solid electrolytes (SEs) for constructing a stable and passivating interphase becomes a sensible choice, benefiting from impermeably physical characteristic of the solid itself.[8] Among various types of SEs, the sulfide-based inorganic solid electrolytes

have attracted ever-increasing attention for all-solid-state lithium batteries (ASSLBs) owing to their high ionic conductivities at room temperature (e.g., $Li_7P_3S_{11}$:17 mS cm^{-1}, $Li_{10}GeP_2S_{12}$: 12 mS cm^{-1}),[9] which is comparable to the organic liquid electrolytes (10 mS cm^{-1}).[10] And due to their deformable mechanical properties, sulfide-based electrolytes are also easily processed into batteries just by pressing the material at room temperature.[11] These advantages make sulfide-based SEs as one of the most promising SE candidates for the commercialization of high-performance ASSLBs. Unfortunately, based on the narrow electrochemical stability window of sulfide-based SEs, ASSLBs will face severe interfacial issues if it is matched with high-voltage cathode materials (such as $LiCoO_2$,[12] $LiNi_{1-x-y}Mn_xCo_yO_2$,[13] etc.), eventually resulting in unsatisfactory cycle life. These issues include the interfacial side-reactions of sulfide SEs, mutual diffusion of non-Li elements and space-charge layer formation.[14] To overcome these problems, a great variety of coating materials have been utilized to modify the surface of cathode or SE, such as $LiNbO_3$,[15] $Li_4Ti_5O_{12}$,[16] and Li_2MoO_4.[17], etc.. Among them, coated-$LiCoO_2$ (LCO) and $LiNi_{1-x-y}Mn_xCo_yO_2$ (NCM) have achieved acceptable electrochemical performance, eg, Li_2WO_4-$LiCoO_2$/Li_6PS_5Cl,[18] $LiZr_2(PO_4)_3$-$LiCoO_2$/Li_6PS_5Cl,[19] $LiNbO_3$-NCM811/$Li_{10}SnP_2S_{12}$,[20] etc., but most are limited to less than 180 mAh g^{-1} due to the material's own capacity limitation. Recently, Kenji et al. developed a novel amorphous $Li_2Ru_{0.8}S_{0.2}O_{3.2}$ cathode material and achieved a high reversible capacity of about 270 mAh g^{-1}. They cleverly avoid the use of solid electrolyte additive in the cathode using the good ductility and conductivity of $Li_2Ru_{0.8}S_{0.2}O_{3.2}$ to construct favorable interfaces. However, the eliminating of solid electrolyte additive form the cathode also results to the requirement of high operating temperature (100 °C) and poor rate capability.[21] The challenge to further improve the electrochemical performance and low the operating temperature by increasing the ionic conductivity of the lithium-rich layered oxide cathodes remains. Introduction of sulfide electrolyte to the composite cathodes has been proved to be an effective strategy to increasing the ionic conductivity of the cathodes. Thus, the constructing of stable interfaces with favorable ionic conductivity between lithium-rich layered oxide cathode and SEs is still a significant challenge for the application of lithium-rich layered oxide cathode to ASSLBs.

In this work, Li_2RuO_3 (LRO), an intriguing lithium-rich layered material, was selected as the cathode material to fabricate ASSLBs with sulfide-based SE to explore the interfacial properties between LRO and sulfide solid electrolytes, and the stability of the anionic redox reaction in ASSLBs. Here, we demonstrated for the first time the feasibility of using SE as a

prospective alternative strategy to create a stable and passivated CEI, which leads to outstanding electrochemical performance. Li_2RuO_3-based ASSLBs show a high reversible capacity of 257 mAh g^{-1} at 0.05 C and excellent cycling stability with 90% capacity retention after 1000 cycles at 1C. A comprehensive experimental analysis combined with density functional theory (DFT) calculations demonstrates the passivating properties of the interface between Li_2RuO_3 and sulfide solid electrolytes, which is beneficial to maintain reversible oxygen redox reaction during long-term cycling, and mitigate the voltage decay, thus give rise to superior electrochemical performance.

2. Results and discussion

2.1. Electrochemical performance

Structure and morphology of LRO particles are shown in **Figure S1**, which are consistent with previous studies.[22] The X-ray diffraction (XRD) pattern of LRO is shown in **Figure S1a**. All the peaks can be perfectly matched to the monoclinic with C2/c space group. The scanning electron microscopy (SEM) image shows that LRO particles possess a uniform particle size of about 1 to 2 μm, as displayed in **Figure S1b**. The transmission electron microscopy (TEM) image (**Figure S1c and d**) shows clear lattice fringes with a lattice spacing of 0.484 nm, corresponding to the (002) planes of the monoclinic LRO.

To obtain high-performance ASSLBs, $Li_7P_3S_{11}$ (LPS) was used as bulk electrolyte, and Li-In was selected as the anode. As-synthesiszed uncoated LRO particles were mixed with Li_6PS_5Cl (LPSCl) and acetylene black for the cathode. A schematic diagram of the LRO-LPSCl-AB|LPS|Li-In ASSLBs is shown in **Figure 1a**. Before electrochemical cycling, the cells were formationly cycled at a low current density of 0.05 C (~10 mA g^{-1}) between 2.0 V and 4.3 V (vs Li/Li^+) at 60 °C for 10 cycles (**Figure 1b**). It can deliver a high first-cycle discharge capacity of 220 mAh g^{-1} and coulombic efficiency (CE) of 84.2%. After formation cycling, the reversible specific capacity increases to 257 mAh g^{-1} with a CE of 99.6% at the 10^{th} cycle, which is comparable to the electrochemical performance of LRO in liquid batteries.[22b, 23] Upon increasing the current density to 0.1C (~20 mA g^{-1}), the cell exhibits an initial discharge capacity of 230 mAh g^{-1} and 98.2% capacity retention after 100 cycles (**Figure 1c** and **S3a**). Furthermore, **Figure 1d and S4** shows the rate capabilities of ASSLBs at 0.05C, 0.2C, 0.5C, 1C, 1.5C, 2C and 5C. Even at the highest current density of 5C, LRO exhibits a specific capacity up to 98 mAh g^{-1}. When the current returns to 0.05C, the capacity of LRO can be fully recovered to 250 mAh g^{-1}, remaining stable in subsequent cycles. These results demonstrated excellent rate performance of LRO in ASSLBs. More importantly, LRO-

LPSCl-AB|LPS|Li-In ASSLBs can deliver a higher initial discharge capacity of 210 mAh g^{-1} at 1C (~200 mA g^{-1}) in **Figure 1e** and **S3b**. After 1000 cycles, the reversible capacity still has 189 mAh g^{-1}, retaining ~90% initial capacity, and the CE is always close to 100%. The shape of the voltage profiles did not change significantly during cycling, only with a slight voltage fade. On the contrary, the LRO cell with liquid electrolyte exhibits severe capacity and voltage decay accompanied by a gradual decrease of coulombic efficiency, and capacity retention is only 48.7% after 995 cycles (**Figure S5**). In order to better emphasize the excellent electrochemical performance, **Figure 1f** compares our results and the latest electrochemical performance for bare and coated LCO, NCM in state-of-the-art sulfide-based ASSLBs (see the more detailed comparison of electrochemical performance including cell design and operating conditions in **Table S1**). It is observed that the performance of LRO-LPSCl-AB|LPS|Li-In ASSLB is more attractive in term of higher reversible capacity, as well as long-term cycling stability. To clarify the working principle of LRO-LPSCl-AB|LPS|Li-In ASSLB cycling performance, we will present a comprehensive analysis of composite cathodes in structure and electrode-electrolyte interface in the following part.

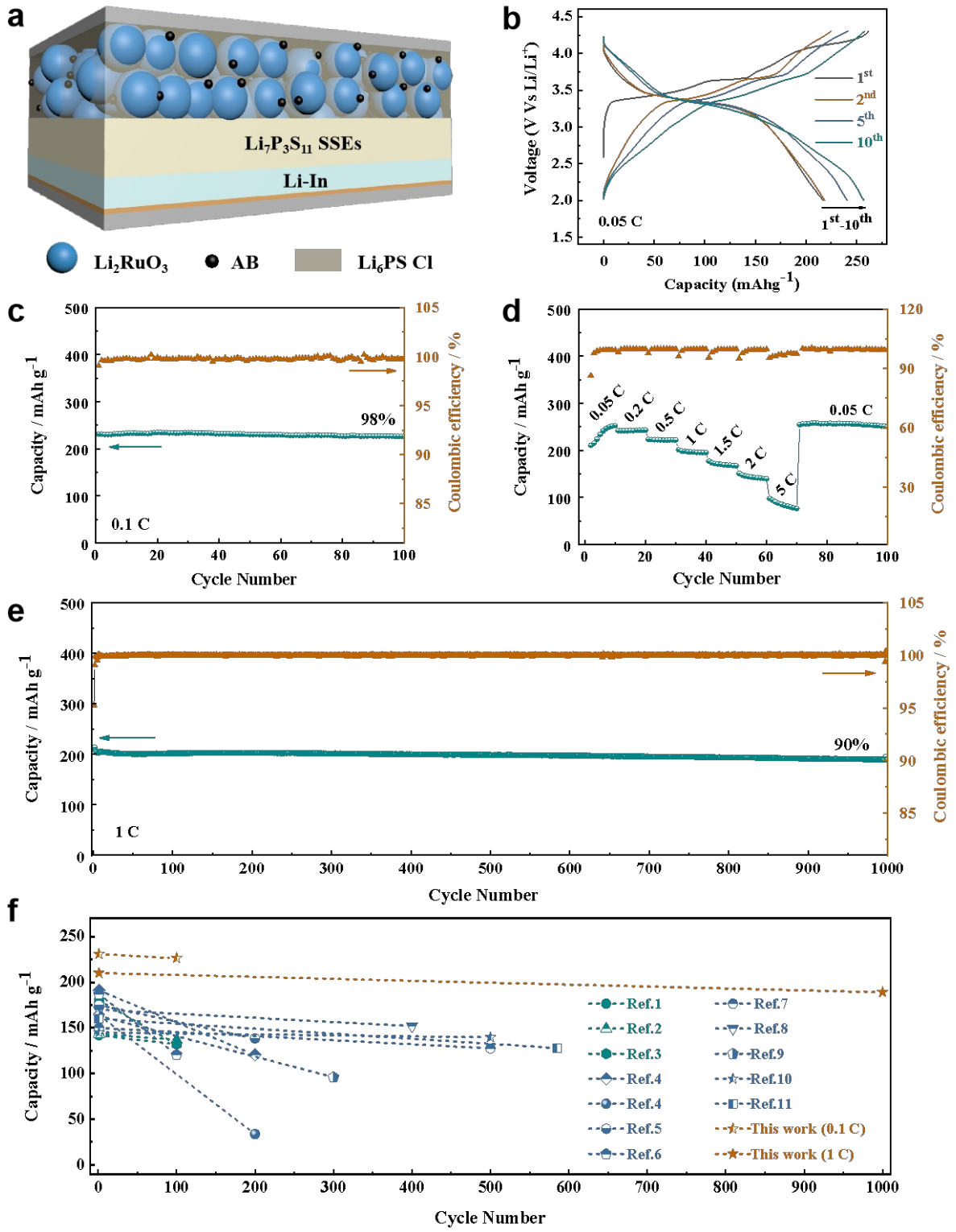

Figure 1. Electrochemical characterization. a) The schematic diagram of the ASSLBs. In the composite positive electrode layer, the LRO (blue balls) and AB (little black balls) are surrounded by the LPSCl matrix (light brown cuboid). LPS was used in the electrolyte layer, and Li-In was selected as the anode. b) Voltage profiles of LRO-LPSCl-AB|LPS|Li-In ASSLBs formation cycling from the 1st to the 10th cycle at 0.05C. c) Cycling performance of LRO in ASSLBs at 0.1C. d) Rate capability of LRO ASSLBs. e) Cycling stability curves of

LRO in ASSLBs at 1C. All cells are cycled between 2.0 and 4.3V (vs Li/Li^+) at 60℃. f) Comparison of electrochemical performance of LRO with currently commercialized layered oxide cathode at the state-of-the-art ASSLBs reported in the literatures. A more detailed comparison of electrochemical performance including cell design and operating conditions are displayed in Table S1.

2.2. Structural evolution of LRO during the initial and second cycles

In-situ X-ray diffraction (XRD) was performed to monitor the structural evolution of LRO in ASSLBs for the initial and second cycles, as shown in **Figure 2**. To emphasize the structural evolution, some representative points (traces a-h in corresponding voltage profile) were highlighted in the direct observation XRD patterns, and the contour plots of LRO (002) diffraction peak was presented with the color depth representing the diffraction intensity. It can be seen that a set of diffraction peaks corresponding to LPSCl SE can be observed at 25.5°, 30°, 31.4°, 44.9° and 52.4°, which did not change during cycling, inferring the good structure stability of bulk LPSCl.[11b] Before 3.74 V, the LRO transformed from pristine monoclinic C2/c phase (point a) to Li deficient C2/c phase ($Li_{1.4}RuO_3$, point b), with the (002) diffraction peak slightly shifted to a low angle.[24] On further oxidation to about 4.05 V (point c), the Li deficient C2/c phase changed to the R-3 phase ($Li_{0.9}RuO_3$).[25] Then, it was observed that no new phase was formed and only the continuous shifting of the (002) peak to a higher angle revealed a solid−solution reaction from 4.05 V to the end of charge at 4.3 V (point d).[22b] Subsequently, two transitions (R-3 phase and Li deficient C2/c phase) were observed with further discharging to 2.0 V (point e) and the second cycle (point f, g).[22b] As expected, these results with multiple phase transitions of LRO during ASSLBs charging and discharging could be analogous to the LIBs system reported in literature,[26] indicating that changes in electrolyte composition have little effect on the structural evolution of LRO. Replacing the liquid electrolyte with SEs, the most direct impact on the cell originates from the interface, suggesting that the interface features between LRO and LPSCl have a crucial role in maintaining the ultra-long cycle stability. Therefore, we will shift research focus towards structural evolution to the electrode-electrolyte interface.

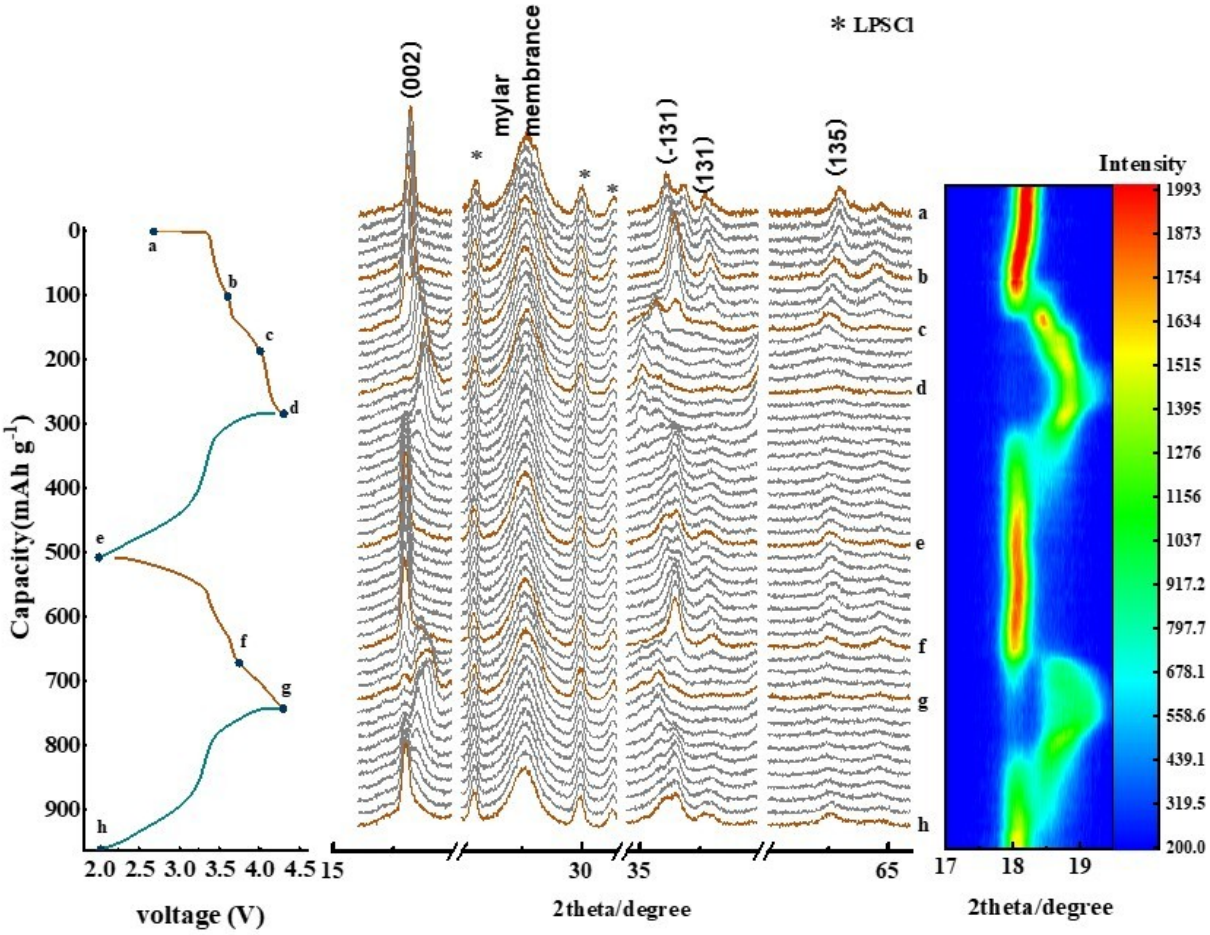

Figure 2. Corresponding voltage profile of LRO in ASSLBs and in-situ XRD analysis of LRO during the first and second charge-discharge processes in ASSLBs. In addition, the contour plots with the color depth representing the diffraction intensity.

2.3 The electrochemical stability of electrode-electrolyte interface

2.3.1. X-ray photoelectron spectroscopy

In order to clarify the interfacial compatibility between LRO and LPSCl, X-ray photoelectron spectroscopy (XPS) was conducted to monitor the interfacial evolution. The surface of all the samples were cleaned by Ar^+ sputtering to eliminate the surface contamination. **Figure 3a and 3b** show the XPS spectra of the S 2p and P 2p for the pristine and the cycled composite cathodes at different states, respectively. The S 2p spectrum of argyrodite LPSCl consists of a doublet with S $2p^{3/2}$ at 161.3 eV, and an extra doublet at 160 eV can be attributed to Li_2S, which comes from the residual reactants during the synthesis of LPSCl.[27] At the second fully discharged state (2.0 V), to fit the spectrum a new doublet at 163.3 eV is required, which can be assigned to P-S-P of polysulfide, indicating the LPSCl SE slightly decomposition. Afterwards, the S 2p spectrum spreads to higher binding energy after

50 cycles, accompanied by an increase of the relative contents of the polysulfide signals at 163.3 eV (P-S-P) and 162 eV (P=S).[28] Moreover, S 2p peaks after 200 cycles show additional peaks at higher binding energy which can be assigned to a trace amount of sulfite (167eV) and large amount of sulfate (169 eV).[29] However, after 400 cycles, the intensities of by-products peaks don't increase further, suggesting the formation of a stable and passivating electrode-electrolyte interphase. Analogous to the S 2p spectra, also here, the P 2p spectrum of the sample mentioned above show similar signal evolution. Compared with the P 2p spectrum of pristine LPSCl (131.7 eV), the spectra of the cycled electrodes show extra doublets at 132.7 eV and 133.9 eV, which can be assigned as phosphorous polysulfide (correlated with the same compounds already mentioned for S 2p spectrum) and phosphate respectively.[28a] In the corresponding electrochemical process, the P 2p spectrum also support the conclusions drawn from the S 2p spectrum regarding the gradually stable electrode-electrolyte interphase after 200 cycles. Therefore, the XPS analysis provides evidence that SE decomposition arises during the electrochemical process, and then the composition and content of the by-products (e.g., polysulfide, phosphate, sulfates, and sulfites) stabilize gradually after multiple cycles, forming a stable and passivating interphase between LRO and SE. This is in agreement with excellent capacity retention of LRO-LPSCl-AB|LPS|Li-In ASSLBs.

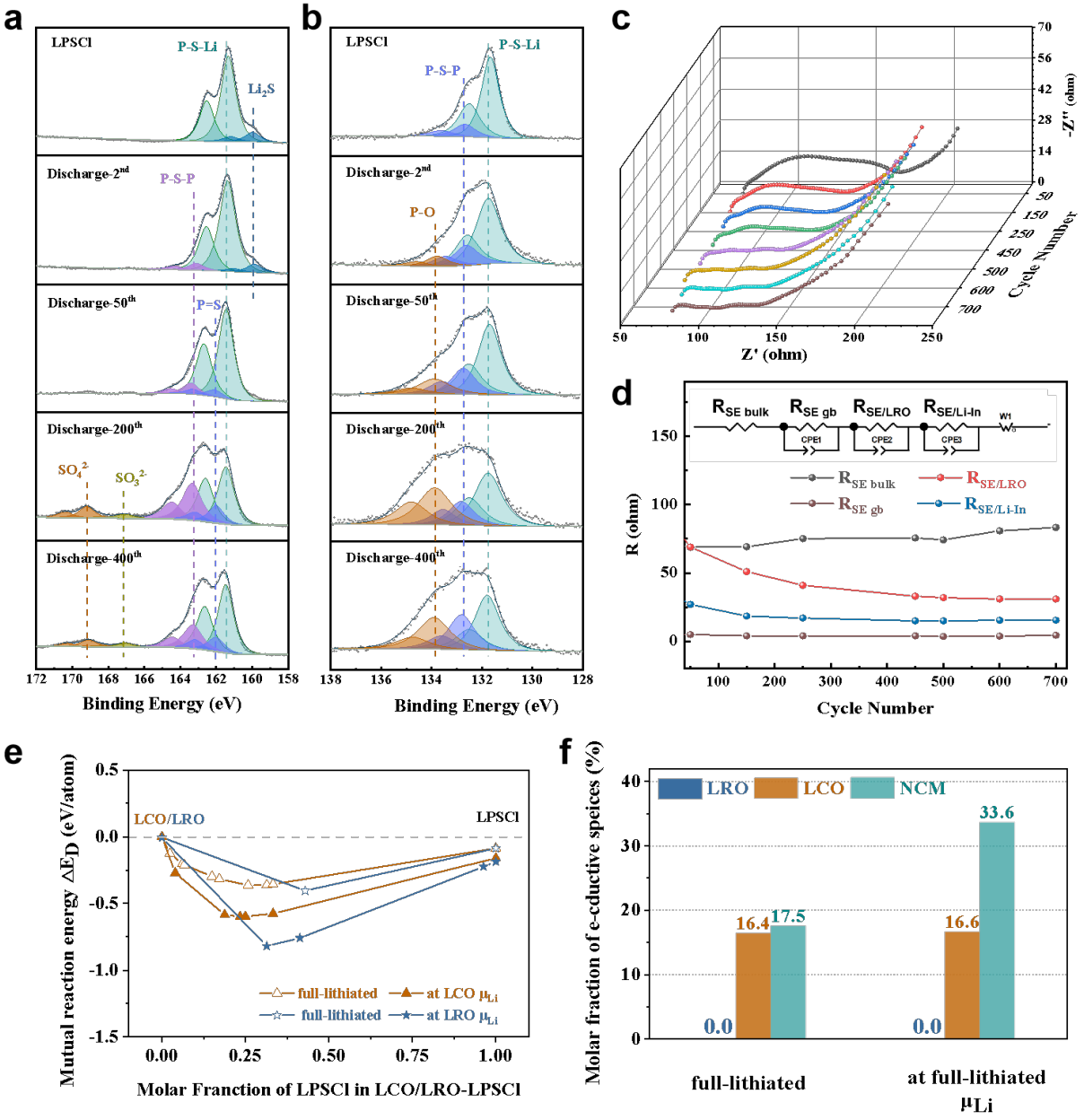

Figure 3. S 2p (a) and P 2p (b) XPS spectra of composite cathodes and after 2nd, 100th, 200th, 400th discharging. (c) Nyquist plot of the impedance spectrum during the cycling. (d) The evolution of the above four resistances obtained by fitting the impedance spectra during cycling. $R_{SE,bulk}$, $R_{SE,gb}$, $R_{SE/LRO}$ and $R_{SE/Li-In}$ represent volume resistance of the solid electrolyte, grain boundary resistance of the SE, the SE/LRO interface resistance, and SE/Li-In interface resistance, respectively. The equivalent circuit model shows on the top part. (e) The mutual reaction energy of the interface between LPSCl and LRO/LCO. (f) The molar fraction of the species with band gap little than 0.5 eV in the phase equilibrium at full-lithiated state of the LRO/LCO/NCM and at Li chemical potential μLi corresponding to the initial charge voltage.

2.3.2. Operando electrochemical impedance spectroscopy

To evaluate the stability of the electrode-electrolyte interphases during long-term cycling, operando electrochemical impedance spectroscopy (EIS) was performed **(Figure 3c)**. Instead of steadily increasing throughout the cycling process as in LIBs (**Figure S6)**, the impedance gradually decreases at first and then stabilizes after 250 cycles, resulting in excellent cycling stability of the ASSLBs. Subsequently, all spectra were fitted with an equivalent circuit model to quantify the interface resistance of each state. A typical impedance spectra model (Nyquist plot) of the ASSLBs during cycling is shown in **Figure S7**. The high frequency semicircle corresponds to the grain boundary resistance of the SE ($R_{SE\ gb}$, 1~0.1 MHz), the middle frequency semicircle relates to the SE/LRO interface resistance ($R_{SE/LRO}$, ~ kHz) and the relative lower frequency should be SE/the anode interface resistance ($R_{SE/Li\text{-}In}$, ~ 1 Hz).[30] **Figure 3d** depicts the value of corresponding resistance by fitting the impedance data. It shows that the $R_{SE\ gb}$ of the ASSLB remains the same, and the bulk resistance of electrolyte ($R_{SE\ Bulk}$) shows very slightly increase even after 700 cycles, indicating the great stability of the bulk solid electrolyte material. $R_{SE/Li\text{-}In}$ fluctuates slightly in early cycles, but remains below 20 Ω thereafter, implying a stable interface between LPS and Li-In alloy. The most significant change in impedance occurs at the interface between the active material and the electrolyte. $R_{SE/LRO}$ decreases rapidly during the first 250 cycles, from 69 Ω to 43 Ω, and then gradually stabilizes in the subsequent cycles. The rapid decrease of $R_{SE/LRO}$ during early cycles indicates that a passivating low-resistance interphase layer forms between LRO and SE, consistent with the XPS results.

2.3.3. DFT calculation

To obtain further insights into the formation of the passivating electrode-electrolyte interface layer between LRO and LPSCl, a phase equilibrium analysis of this pseudo-binary component at the fully-lithiated state of cathode and at Li chemical potential μLi, was carried out and compared to a phase equilibrium analysis of conventional layered cathodes such as LCO and NCM, as shown in **Figure 3e, S8** and **Table S2**. It is found that the LRO/LPSCl interface is thermodynamically unstable and undergoes spontaneous decomposition reactions just like the interface of LCO/LPSCl and NCM/LPSCl. In addition, from the decomposition products listed in Table S2, it can be found that Li_2SO_4 and Li_3PO_4 are formed via chemical and electrochemical reactions between LRO and LPSCl, which is also consistent with the

XPS results. In general, an electronically insulating and ionically conductive interfacial layer can form a stable and passivating interface between cathode and SEs.[31] Thus, the mole fraction of phases formed in the phase equilibrium with band gap smaller than 0.5 eV for the LRO/LPSCl interface, which are likely to be an electronic conductor existing at interphase layer, are counted in detail as shown in **Figure 3f**. As a comparison, the phase equilibrium between LPSCl and LCO/NCM was also investigated systematically. It can be found that the mole fraction of electron conducting species (i.e. with low band gap) formed at the LCO/NCM-LPSCl interface is sufficient (LCO: 16.4, 16.6%, NCM: 17.5, 33.6% at full-lithiated and μLi, respectively) to make it a mixed ionic and electronic conducting (MIEC) interphase layer, which is regarded a key factor leading to the degradation of battery cycling performance.[32] By contrast, no electronic conducting species are formed at the interphase between LPSCl and LRO at the fully lithiated state of LRO, indicating that this interphase has the ability to passivate the electrode-electrolyte interface achieving long-term cycling stability.

2.3.4. Cross-sectional SEM and corresponding energy dispersive spectroscopy (EDS) elemental mapping

The morphological evolution of the cathodes composite interface for the pristine and after 100 cycles were examined by cross-sectional SEM and corresponding energy dispersive spectroscopy (EDS) elemental mapping in **Figure 4**. **Figure 4a** reveals that LRO particles (light grey color) are surrounded by a matrix consisting of LPSCl and acetylene black particles (dark grey color) in the pristine cathode. After 100 cycles, no significant crack formation is observed and the initial particle morphology is maintained in the cathodes composite in **Figure 4b**. **Figure 4c-h** show the SEM-EDS mapping results of the elemental distribution of Ru (Figure 4d and 4g) and S (Figure 4e and 4h) of the pristine and cycled cathode (**Figure 4c-h**), it can be clearly observed that Ru (from the cathode), and S (from sulfide electrolyte) elements were conformal distributed in cathode side and sulfide electrolyte side even after 100 cycling, indicating good interfacial stability between the cathode and sulfide SE. It was reported that the S could easily diffuse into NCM particles in ASSLBs, which led to continuous interfacial reaction and deterioration of electrochemical performance.[14a] On the contrary, no apparent element inter-diffusion is observed in this cell and the interface between Ru and S remains sharp. Therefore, a stable interphase is formed between LRO and LPSCI, which inhibits further side reactions, consistent with the DFT results.

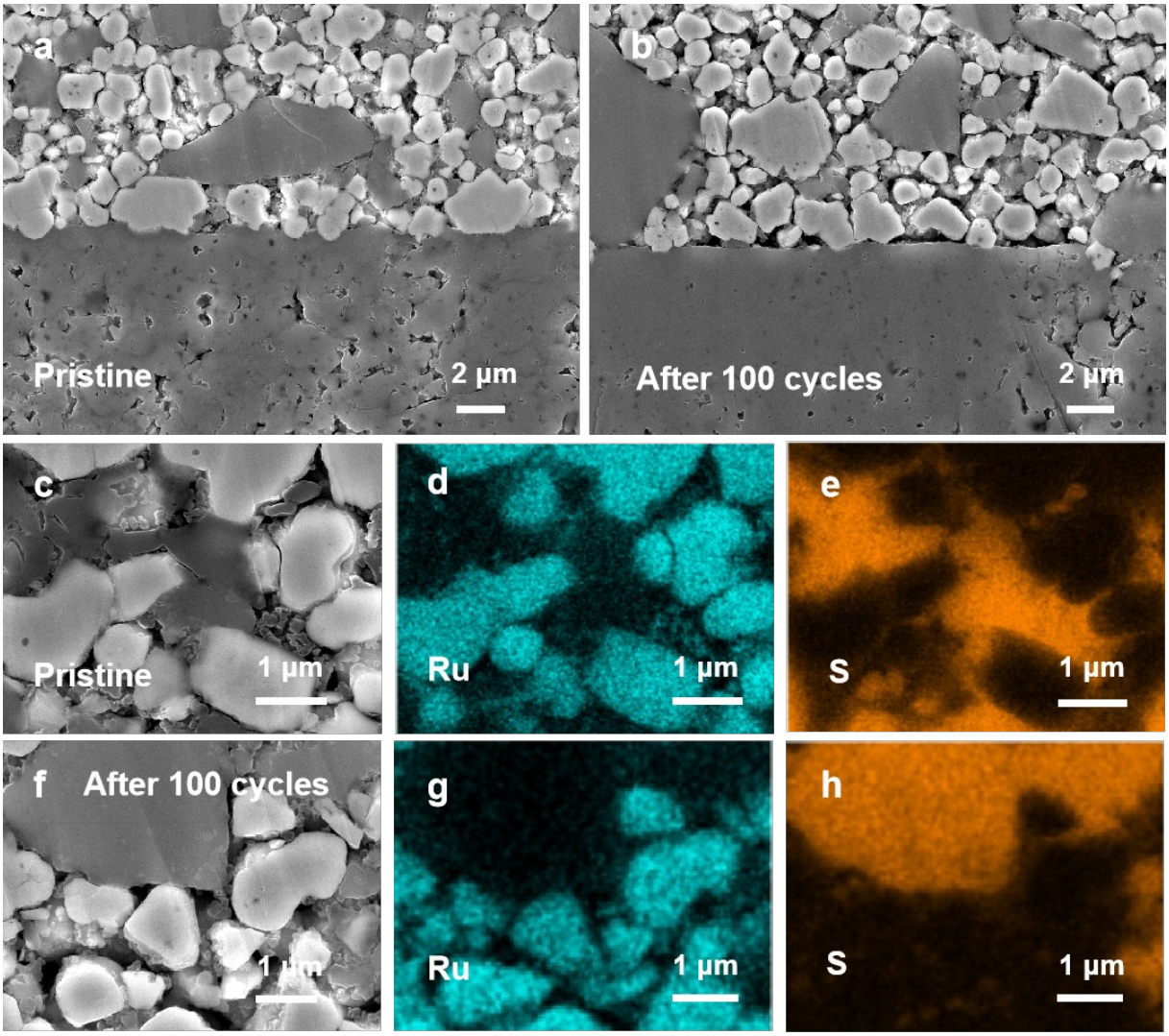

Figure 4. Cross-sectional SEM and corresponding EDS elemental mapping of the electrodes at the pristine and after 100 cycles. Cross-sectional SEM images of the electrodes at the pristine (a) and after 100 cycles (b). Cross-sectional SEM images of larger magnification (c) and corresponding Ru (blue, d) and S (orange, e) maps of the region (c) of the electrodes at the pristine. Cross-sectional SEM images of larger magnification (f) and corresponding Ru (blue, g) and S (orange, h) maps of the region (f) of the electrodes after 100 cycles.

2.4 Reversible Oxygen Redox

As mentioned above, ASSLBs made of LRO and LPSCl SE can achieve outstanding reversible capacities of 257 mAh g^{-1}. To fully understand the electrochemical reaction mechanism of LRO in ASSLBs, it is necessary to analyze the charge compensation mechanism of cathode materials. It is worth noting that the theoretical capacity expected by the charge compensation of cationic Ru^{4+}/Ru^{5+} redox species in LRO is only 164 mAh g^{-1}, which indicates that the extra capacity in ASSLBs are from other redox reactions.[21] Based on

the XPS results, the electrochemical decomposition of SE possibly contribute to the capacity of the ASSLBs. To test this, the LPSCl-AB composite electrodes were prepared and the corresponding electrochemical performance were characterized under the same test conditions as LRO ASSLBs **(Figure S9)**. The results show that the contribution from LPSCl decomposition to the overall battery capacity is negligible (less than 3mAh g^{-1}), thus anionic reactions may provide these extra capacities.

Here, mapping of resonant inelastic X-ray scattering (mRIXs) of the O-K edge provides the direct evidence regarding reversible oxygen redox of LRO during the long-term cycling of the ASSLB.[33] Previous studies have shown that lattice oxidized oxygen has two coexisting fingerprint features on the RIXS map at the charged states: (i) a sharp feature around 531 eV excitation and 524 eV emission energy, (ii) a low-energy-loss feature close on the elastic line at the same excitation energy.[23b, 34] **Figure 5a** and **b** display the full O K edge RIXS maps of the LRO electrode at pristine LRO electrode and at 11^{th} cycle charged to 4.3 V, respectively. The two characteristics features of the above-mentioned appear on the 11^{th} delithiation, highlighted by the red arrows and the yellow circles in Figure 5a, respectively. The spectroscopic results confirm the existence of the reversible oxygen redox in LRO ASSLBs. Moreover, further comparison of the RIXS cuts at 531 eV excitation energy of all samples at the fully charged state and their corresponding discharges state (light gray) are shown in **Figure 5c**. The two characteristic features representing the oxidized lattice oxygen in the charged states are clearly marked out (red arrows blue coil). It should be noted that the features representing oxidized oxygen are absent first two cycles (activation process), and start to appear at the 11^{th} charged state and remain until 600 cycles. This suggests the reversible oxygen redox maintains during the long-term cycling of the LRO ASSLBs.

Numerous studies have reported that lithium-rich cathode materials are subject to inevitable oxygen loss during long-term cycling resulting in vacancies and large pores formation.[1b, 7] In addition, continuous migration of oxygen vacancies and transition metal ions result in microcrack evolution in a single crystal.[35] The LRO particles also observed obvious cracks in ASSLBs after 300 cycles **(Figure S10)**. Thus, active materials expose more fresh surfaces. In LIBs, the flowing electrolyte can contact with these fresh interfaces and generate more interfacial side reactions, promoting further oxygen loss. Unlike conventional liquid electrolyte, the SE does not flow and permeate into porous materials, which lead to less continuous parasitic interfacial reactions and oxygen loss. Interestingly, although the LRO particles are cracked, its long-term cycling performance has not been obviously affected,

which anomalous phenomenon deserves further exploration in the next work. Moreover, thanks to the passivation properties of the LRO/LPSCl interphase, there is no continuous growth of the CEI layer during the long-term cycling. As a result, the oxygen redox is maintained for at least 600 cycles and a super-stable electrochemical performance is achieved. These conclusions can be schematically highlighted in Figure 5f. The stable LRO/SE interface passivated by the interphase does a great job keeping the activity of oxygen redox.

In addition, it was demonstrated that oxygen loss played a critical role in voltage fade.[1b] **Figure 5d** shows a comparison diagram of the normalized discharge curves at the 11th and 200th cycles of LRO in ASSLBs and LIBs at 0.1C between 2.0-4.3 V. The voltage drops of the normalized discharge curve of the 200th cycle compared with the 11th cycle in ASSLBs is obvious less than LIBs. Furthermore, **figure 5e** shows that the average voltage decay for ASSLBs (300 mV) after 200 cycles is significantly less than LIBs (700mV). Therefore, benefiting from the long-term reversible redox of the lattice oxygen of LRO in ASSLBs, the inherent voltage decay of lithium-rich materials has also been greatly alleviated.

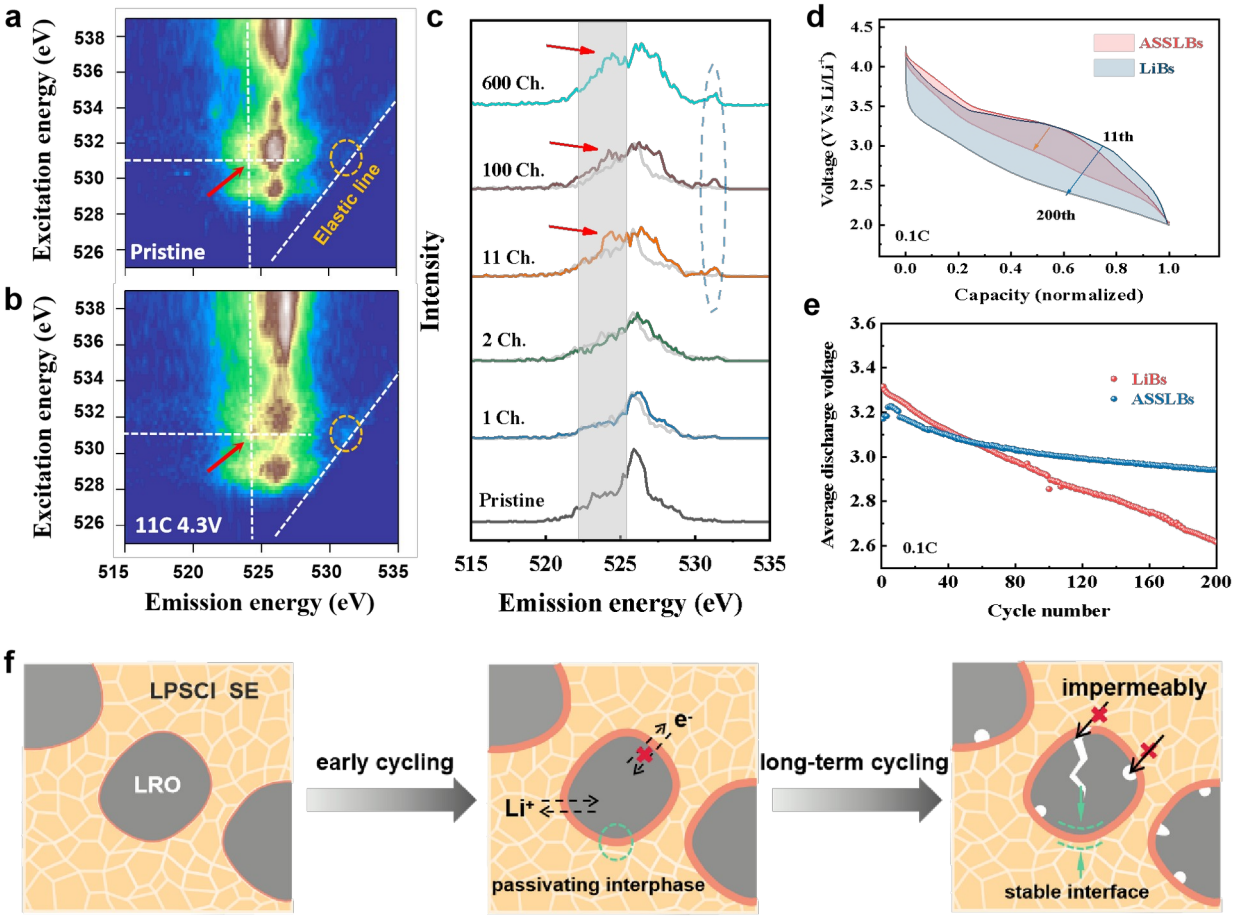

Figure 5. O-K mRIXS of LRO electrodes at the pristine (a) and upon 11th charge states (b). The red arrows and the yellow circle indicated the features of anionic oxygen redox. (c) The

RIXs spectra extracted at 531 eV excitation energy of several samples in the fully charged states and corresponding discharges states (light gray plot). The intensity in the red arrow and the blue coil corresponds to the oxidized oxygen triggered by oxygen redox reaction at the charged state. “1 Ch.” represents first charged state. (d) Comparison of the discharge curves of LRO in LIBs and ASSLBs from cycles 11 to 200, respectively. (e) Comparison of the average voltage of LRO in LIBs and ASSLBs at 0.1C cycled between 2.0-4.3V. (f) Schematic illustration of the interfacial passivating mechanism and effects of the reversible oxygen redox.

3. Conclusion

In this work, we fabricated the LRO and LPSCl SE into ASSLBs achieving outstanding reversible capacities and remarkable cycling performance. XPS and cross-section SEM characterizations combined with DFT calculations, reveal that the properties of interfacial reaction products play a critical role in the interface stability in all-solid-state batteries. The electronic insulating phases formed between Li_2RuO_3 cathode and sulfide electrolyte is passivating against further electrochemical oxidation to stabilize the interface. EIS results confirm the formation of a stable interphase with a stable interfacial impedance during long-term cycling. Moreover, the reversible oxygen redox activity can be well-maintained during long-term cycling as revealed by mRIXS, which is beneficial to the reversibly exploit the anionic redox reaction and effectively alleviate the voltage decay, thus achieve outstanding electrochemical performance. Our discovery offers a good guideline for rationally design the lithium-rich cathode/sulfide electrode interface toward high energy density ASSLBs.

4. Experimental Section

Synthesis: LRO samples were prepared by conventional solid-state reaction as previously reported. Stoichiometric amounts of RuO_2 (Sigma-Aldrich 99.9%) and Li_2CO_3 (Sigma-Aldrich 99.0%) with a 10 wt% excess were mixed by using ball-milling at a rate of 400 rpm for 4 h, and then the obtained precursor was heated at 900℃ for 12h with a slow heating rate in air. LPSCl samples were prepared by Li_2S (Alfa Aesar, 99.9%), P_2S_5 (Sigma-Aladdin, 99%) and LiCl (Sigma-Aladdin, 99.9%) in the prescriptive molar ratio mixing at 300 rpm for 24 h. The mixture was then calcined at 550 ℃ for 6 h under Ar atmosphere. Similarly, to synthesize LPS, the same Li_2S and P_2S_5 as raw materials were ball milled at the same speed

and time. Then the calcined conditions are 210 ℃ for 3h and 250 ℃ for 1h with a heating rate of 1 °C min^{-1} in Ar atmosphere.

Cell assembly and electrochemical characterization: In this study, LRO without any modification treatment were mixed with LPSCl and AB as cathode materials. LPS was used in the electrolyte layer, and Li-In was selected as the anode. The LRO-LPSCl-AB composite cathode was prepared and ground by hand mixing the as prepared LRO powder with LPSCl and AB with a weight ratio of 60 : 38 : 2 in an agate mortar for 60 min. ASSLBs fabricated using LRO-LPSCl-AB composite as the cathode, LPS as the solid electrolyte, and Li-In alloy as the anode. For the assembly of LRO-LPSCl-AB|LPS|Li-In cells, a mass of 100 mg of the LPS SE powder was first placed into a polycarbonate tube with a 10 mm diameter, followed by cold pressing under 300 MPa to form the solid electrolyte layer with thicknesses of about 750 μm. After that, a total of 5.2 mg of LRO-LPSCl-AB composite powder was homogeneously distributed on one side of the as-formed LPS SE layer and then pressed together under 360 MPa. The mass loading of the LRO active material is 4 mg cm^{-2}. Li-In alloy foil with a molar ratio of 3:7 as the anode composite was attached to the other side of the electrolyte by pressing under 120 MPa. All cell processes were carried out in an argon-filled glove box. The ionic conductivity of LPSCl and LPS shows 2.4×10^{-3} S cm^{-1} and 1.2×10^{-3} S cm^{-1} at room temperature (**Figure S2**), respectively, which is similar to the reported values.[11b, 36] Galvanostatic charge-discharge tests of the ASSLBs were conducted on the Land battery test system (LAND CT- 2001A, Wuhan, China) at different current densities (based on 1C=200 mA g-1) under 60 °C or RT. The voltage window was set as 1.4-3.7 V vs Li-In (2.0-4.3 V Vs Li/Li^+). EIS was recorded on the Autolab PGSTA302 electrochemical workstation (Eco Chemie, Netherland) in a frequency range of 10 mHz to 1 MHz with a signal amplitude of 50 mV.

Characterization: XRD was collected on Rigaku Corporation (Japan) equipped with Cu Ka radiation (λ = 1.5406 Å), and in-situ XRD patterns were carried out on a Bruker D8 Discover X-ray diffractometer equipped with a Cu Target X-ray tube and a VANTEC-500 planar detector. A specially designed coin cell with holes for beam pass was employed for in-situ XRD testing. The cell was cycled at a low current density (0.05C) by using the Neware battery test system during the experiment. XPS measurements were conducted using K-Alpha+ (Thermo Scientific) with a monochromatic Al Ka source (1486.6 eV) at 15 KV and

15 mA. The morphology of the synthesized LRO powder was characterized by SEM (MERLIN Compact ZEISS, Germany) and TEM (Tecnai F30, Philips-FEI, Netherlands), respectively. For cross-sectional SEM (JEOL, JSM-7900F, Japan) and EDX observations, the sample was prepared by a cross section polisher ((JEOL, IB-19520CCP, Japan). All samples were collected in Ar-atmospheres and transferred into the SEM without exposure to air. mRIXS was collected at the high-efficiency iRIXS endstation at beamline 8.0.1 of the Advanced Light Source (ALS) at Lawrence Berkeley National Laboratory (LBNL).

Phase equilibrium Analysis: The chemical and electrochemical stability of the interfaces exiting in the composite cathode were systematically analyzed by the scheme proposed by Mo et al..[37] The details were described the supporting information. Based on the scheme proposed by Mo et al.,[37] the interface can be regarded as a pseudo-binary composition consisted by A and B.

$$C_{interface}(C_A, C_B, x) = x \cdot C_A + (1-x) \cdot C_B$$

where, x is the fraction of A, C_A and C_B is the component of A and B. The total energy of this pseudo-binary composition can be described as the liner combination of A and B.

$$E_{interface}(A, B, x) = x \cdot E(A) + (1-x) \cdot E(B)$$

Where, $E_{interface}(A, B, x)$, is the total energy, $E(A)$ and $E(B)$ and is the energy of ground state of A and B. The decomposition energy, $\triangle E_D \ \ phase$, is described as follows

$$\triangle E_D \ \ phase = E_{eq}(C) - E(phase)$$

$E_{eq}(C)$ and $E(phase)$ is the energy of phase equilibria and phase. The phase equilibria at the composition C corresponding to the energy minimum $E_{eq}(C)$ were identified by comparing the energy of all relevant phases in their compositional space. The chemical stability of A and B can be evaluated by the decomposition energy calculated from the equation as follows:

$$E_D(A, B, x) = E_{eq}\left(C_{interface}(C_A, C_B, x)\right) - E_{interface}(A, B, x)$$

The mutual reaction energy of A and B, $\Delta E_{D,mutual}(A, B, x)$, is calculated as:

$$\Delta E_{D,mutual}(A, B, x) = \Delta E_D(A, B, x) - x \cdot \Delta E_D(A) - (1-x) \cdot \Delta E_D(B)$$

The electrochemical stability can also be estimated by inducing the correction term of the electrode potential $\varnothing$ which considered as a part of the Li chemical potentialμ_{Li}.

$$\mu_{Li}(\varnothing) = \mu_{Li}^0 - e\varnothing$$

where μ_{Li}^0 is the chemical potential of Li metal, and the applied potential $\varnothing$ was referenced to the Li metal.

$$\Delta E_{D,mutual}^{open}(A,B,x,\varnothing)=\Delta E_{D}^{open}(A,B,x,\varnothing)-x\cdot\Delta E_{D}^{open}(A,\varnothing)-(1-x)\cdot\Delta E_{D}^{open}(B,\varnothing)$$

Mole fraction of the e-conductor exiting in the interphase layer: The products with band gap smaller than 0.5 eV might be an e-conductor exit in the interphase, which can induce the electrochemical reaction between SE and cathode. Hence, the mole fraction (f) of e-conductive products, xC, in the total products is calculated as follows,

$$aA+bB\rightarrow xC+yD$$

$$f=\frac{x}{x+y}$$

according to the assumption in the MP analysis above $a+b=1$. Here the band gaps of C and D are smaller and bigger than 0.5 eV, respectively.

Since the different mixed ratio of SE in the pseudo-binary composition consisted by SE and cathode, there exist several possible phase equilibriums between sulfide SE and cathode at different mixed ratios. The mole fraction of e-conductive phase is the average of all these possible phase equilibria.

Supporting Information

Supporting Information is available from the Wiley Online Library or from the author.

Acknowledgements

Y. Q. Wu and K. Zhou contributed equally to this work. This work was supported by the National Natural Science Foundation of China (Grants No. 21875196, 21935009 and 22021001), the National Key R&D Program of China (Grant No. 2021YFB2401800) and the Science and Technology Planning Projects of Fujian Province, China (Grant 2019H0003).

Received: ((will be filled in by the editorial staff))

Revised: ((will be filled in by the editorial staff))

Published online: ((will be filled in by the editorial staff))

References

[1] a)G. Assat, J.-M. Tarascon, *Nature Energy* **2018**, 3, 373; b)E. Hu, X. Yu, R. Lin, X. Bi, J. Lu, S. Bak, K.-W. Nam, H. L. Xin, C. Jaye, D. A. Fischer, K. Amine, X.-Q. Yang,

Nature Energy **2018**, 3, 690; c)J. Lee, D. A. Kitchaev, D. H. Kwon, C. W. Lee, J. K. Papp, Y. S. Liu, Z. Lun, R. J. Clement, T. Shi, B. D. McCloskey, J. Guo, M. Balasubramanian, G. Ceder, *Nature* **2018**, 556, 185; d)J.-N. Zhang, Q. Li, C. Ouyang, X. Yu, M. Ge, X. Huang, E. Hu, C. Ma, S. Li, R. Xiao, W. Yang, Y. Chu, Y. Liu, H. Yu, X.-Q. Yang, X. Huang, L. Chen, H. Li, *Nature Energy* **2019**, 4, 594.

[2] a)J. Xu, M. Sun, R. Qiao, S. E. Renfrew, L. Ma, T. Wu, S. Hwang, D. Nordlund, D. Su, K. Amine, J. Lu, B. D. McCloskey, W. Yang, W. Tong, *Nat Commun* **2018**, 9, 947; b)F. Ning, B. Li, J. Song, Y. Zuo, H. Shang, Z. Zhao, Z. Yu, W. Chu, K. Zhang, G. Feng, X. Wang, D. Xia, *Nat Commun* **2020**, 11, 4973.

[3] a)G. Assat, D. Foix, C. Delacourt, A. Iadecola, R. Dedryvere, J. M. Tarascon, *Nat Commun* **2017**, 8, 2219; b)D. Eum, B. Kim, S. J. Kim, H. Park, J. Wu, S. P. Cho, G. Yoon, M. H. Lee, S. K. Jung, W. Yang, W. M. Seong, K. Ku, O. Tamwattana, S. K. Park, I. Hwang, K. Kang, *Nat Mater* **2020**, 19, 419.

[4] a)W. Zuo, M. Luo, X. Liu, J. Wu, H. Liu, J. Li, M. Winter, R. Fu, W. Yang, Y. Yang, *Energy & Environmental Science* **2020**, 13, 4450; b)S. Hu, Y. Li, Y. Chen, J. Peng, T. Zhou, W. K. Pang, C. Didier, V. K. Peterson, H. Wang, Q. Li, Z. Guo, *Advanced Energy Materials* **2019**, 9, 1901795; c)W. Li, B. Song, A. Manthiram, *Chem Soc Rev* **2017**, 46, 3006.

[5] a)B. Jiang, J. Li, B. Luo, Q. Yan, H. Li, L. Liu, L. Chu, Y. Li, Q. Zhang, M. Li, *Journal of Energy Chemistry* **2021**, 60, 564; b)Y. Yue, Y. Ha, R. Giovine, R. Clément, W. Yang, W. Tong, *Chemistry of Materials* **2022**, 34, 1524.

[6] Q. Li, Y. Wang, X. Wang, X. Sun, J. N. Zhang, X. Yu, H. Li, *ACS Appl Mater Interfaces* **2020**, 12, 2319.

[7] a)B. Qiu, M. Zhang, L. Wu, J. Wang, Y. Xia, D. Qian, H. Liu, S. Hy, Y. Chen, K. An, Y. Zhu, Z. Liu, Y. S. Meng, *Nat Commun* **2016**, 7, 12108; b)P. Yan, J. Zheng, Z. K. Tang, A. Devaraj, G. Chen, K. Amine, J. G. Zhang, L. M. Liu, C. Wang, *Nat Nanotechnol* **2019**, 14, 602; c)H. C. Shim, D. Kim, D. Shin, S. Hyun, C. S. Woo, T. Yu, J. P. Ahn, *Phys Chem Chem Phys* **2017**, 19, 1268.

[8] D. H. S. Tan, Y. T. Chen, H. Yang, W. Bao, B. Sreenarayanan, J. M. Doux, W. Li, B. Lu, S. Y. Ham, B. Sayahpour, J. Scharf, E. A. Wu, G. Deysher, H. E. Han, H. J. Hah, H. Jeong, J. B. Lee, Z. Chen, Y. S. Meng, *Science* **2021**, 373, 1494.

[9] a)N. Kamaya, K. Homma, Y. Yamakawa, M. Hirayama, R. Kanno, M. Yonemura, T. Kamiyama, Y. Kato, S. Hama, K. Kawamoto, A. Mitsui, *Nat Mater* **2011**, 10, 682; b)Y. Seino, T. Ota, K. Takada, A. Hayashi, M. Tatsumisago, *Energy Environ. Sci.* **2014**, 7, 627.

[10] S. H. Jung, U. H. Kim, J. H. Kim, S. Jun, C. S. Yoon, Y. S. Jung, Y. K. Sun, *Advanced Energy Materials* **2019**, 10.

[11] a)D. H. Kim, Y.-H. Lee, Y. B. Song, H. Kwak, S.-Y. Lee, Y. S. Jung, *ACS Energy Letters* **2020**, 5, 718; b)L. Zhou, K.-H. Park, X. Sun, F. Lalère, T. Adermann, P. Hartmann, L. F. Nazar, *ACS Energy Letters* **2018**, 4, 265; c)A. Miura, N. C. Rosero-Navarro, A. Sakuda, K. Tadanaga, N. H. H. Phuc, A. Matsuda, N. Machida, A. Hayashi, M. Tatsumisago, *Nature Reviews Chemistry* **2019**, 3, 189.

[12] C.-W. Wang, F.-C. Ren, Y. Zhou, P.-F. Yan, X.-D. Zhou, S.-J. Zhang, W. Liu, W.-D. Zhang, M.-H. Zou, L.-Y. Zeng, X.-Y. Yao, L. Huang, J.-T. Li, S.-G. Sun, *Energy & Environmental Science* **2021**, 14, 437.

[13] C. Wang, S. Hwang, M. Jiang, J. Liang, Y. Sun, K. Adair, M. Zheng, S. Mukherjee, X. Li, R. Li, H. Huang, S. Zhao, L. Zhang, S. Lu, J. Wang, C. V. Singh, D. Su, X. Sun, *Advanced Energy Materials* **2021**, 11, 2100210.

[14] a)X. Li, Z. Ren, M. Norouzi Banis, S. Deng, Y. Zhao, Q. Sun, C. Wang, X. Yang, W. Li, J. Liang, X. Li, Y. Sun, K. Adair, R. Li, Y. Hu, T.-K. Sham, H. Huang, L. Zhang, S. Lu, J. Luo, X. Sun, *ACS Energy Letters* **2019**, 4, 2480; b)G. Liu, Y. Lu, H. Wan, W. Weng, L. Cai, Z. Li, X. Que, H. Liu, X. Yao, *ACS Appl Mater Interfaces* **2020**, 12, 28083.

[15] F. Walther, F. Strauss, X. Wu, B. Mogwitz, J. Hertle, J. Sann, M. Rohnke, T. Brezesinski, J. Janek, *Chemistry of Materials* **2021**, 33, 2110.

[16] N. Ohta, K. Takada, L. Zhang, R. Ma, M. Osada, T. Sasaki, *Advanced Materials* **2006**, 18, 2226.

[17] H. W. Kwak, Y. J. Park, *Thin Solid Films* **2018**, 660, 625.

[18] Z. Sun, Y. Lai, N. lv, Y. Hu, B. Li, S. Jing, L. Jiang, M. Jia, J. Li, S. Chen, F. Liu, *Advanced Materials Interfaces* **2021**, 8, 2100624.

[19] L. Wang, X. Sun, J. Ma, B. Chen, C. Li, J. Li, L. Chang, X. Yu, T. S. Chan, Z. Hu, M. Noked, G. Cui, *Advanced Energy Materials* **2021**, 11, 2100881.

[20] X. Liu, B. Zheng, J. Zhao, W. Zhao, Z. Liang, Y. Su, C. Xie, K. Zhou, Y. Xiang, J. Zhu, H. Wang, G. Zhong, Z. Gong, J. Huang, Y. Yang, *Advanced Energy Materials* **2021**, 11, 2003583.

[21] K. Nagao, Y. Nagata, A. Sakuda, A. Hayashi, M. Deguchi, C. Hotehama, H. Tsukasaki, S. Mori, Y. Orikasa, K. Yamamoto, Y. Uchimoto, M. Tatsumisago, *Science Advances*, 6, eaax7236.

[22] a)A. K. Kalathil, P. Arunkumar, D. H. Kim, J. W. Lee, W. B. Im, *ACS Appl Mater Interfaces* **2015**, 7, 7118; b)B. Li, R. Shao, H. Yan, L. An, B. Zhang, H. Wei, J. Ma, D. Xia, X. Han, *Advanced Functional Materials* **2016**, 26, 1330.

[23] a)R. R. Neelakantaiah, B. B. Dasari, P. M. Ette, K. Ramesha, *ChemElectroChem* **2020**, 7, 328; b)Z. Zhuo, K. Dai, J. Wu, L. Zhang, N. Tamura, Y.-d. Chuang, J. Feng, J. Guo, Z.-x. Shen, G. Liu, F. Pan, W. Yang, *ACS Energy Letters* **2021**, 6, 3417.

[24] D. Mori, H. Kobayashi, T. Okumura, H. Nitani, M. Ogawa, Y. Inaguma, *Solid State Ionics* **2016**, 285, 66.

[25] F. Zheng, S. Zheng, P. Zhang, X. Zhang, S. Wu, Y. Yang, Z.-z. Zhu, *The Journal of Physical Chemistry C* **2019**, 123, 13491.

[26] a)M. Sathiya, G. Rousse, K. Ramesha, C. P. Laisa, H. Vezin, M. T. Sougrati, M. L. Doublet, D. Foix, D. Gonbeau, W. Walker, A. S. Prakash, M. Ben Hassine, L. Dupont, J. M. Tarascon, *Nat Mater* **2013**, 12, 827; b)M. Han, Z. Liu, X. Shen, L. Yang, X. Shen, Q. Zhang, X. Liu, J. Wang, H. J. Lin, C. T. Chen, C. W. Pao, J. L. Chen, Q. Kong, X. Yu, R. Yu, L. Gu, Z. Hu, X. Wang, Z. Wang, L. Chen, *Advanced Energy Materials* **2020**, 10, 2002631.

[27] a)J. Auvergniot, A. Cassel, D. Foix, V. Viallet, V. Seznec, R. Dedryvère, *Solid State Ionics* **2017**, 300, 78; b)S. Ohno, R. Koerver, G. Dewald, C. Rosenbach, P. Titscher, D. Steckermeier, A. Kwade, J. Janek, W. G. Zeier, *Chemistry of Materials* **2019**, 31, 2930.

[28] a)J. Auvergniot, A. Cassel, J.-B. Ledeuil, V. Viallet, V. Seznec, R. Dedryvère, *Chemistry of Materials* **2017**, 29, 3883; b)S. Wang, X. Xu, X. Zhang, C. Xin, B. Xu, L. Li, Y.-H. Lin, Y. Shen, B. Li, C.-W. Nan, *Journal of Materials Chemistry A* **2019**, 7, 18612.

[29] C. Wang, S. Hwang, M. Jiang, J. Liang, Y. Sun, K. Adair, M. Zheng, S. Mukherjee, X. Li, R. Li, H. Huang, S. Zhao, L. Zhang, S. Lu, J. Wang, C. V. Singh, D. Su, X. Sun, *Advanced Energy Materials* **2021**, 11.

[30] a)R. Koerver, I. Aygün, T. Leichtweiß, C. Dietrich, W. Zhang, J. O. Binder, P. Hartmann, W. G. Zeier, J. Janek, *Chemistry of Materials* **2017**, 29, 5574; b)W. Zhang, F. H. Richter, S. P. Culver, T. Leichtweiss, J. G. Lozano, C. Dietrich, P. G. Bruce, W. G. Zeier, J. Janek, *ACS Appl Mater Interfaces* **2018**, 10, 22226.

[31] a)Y. Zhu, X. He, Y. Mo, *ACS Appl Mater Interfaces* **2015**, 7, 23685; b)A. M. Nolan, Y. Liu, Y. Mo, *ACS Energy Letters* **2019**, 4, 2444; c)X. Liu, B. Zheng, J. Zhao, W. Zhao, Z. Liang, Y. Su, C. Xie, K. Zhou, Y. Xiang, J. Zhu, H. Wang, G. Zhong, Z. Gong, J. Huang, Y. Yang, *Advanced Energy Materials* **2021**, 11.

[32] a)A. M. Nolan, Y. Zhu, X. He, Q. Bai, Y. Mo, *Joule* **2018**, 2, 2016; b)J. Li, C. Ma, M. Chi, C. Liang, N. J. Dudney, *Advanced Energy Materials* **2015**, 5.

[33] W. Yang, T. P. Devereaux, *Journal of Power Sources* **2018**, 389, 188.

[34] Z. Zhuo, K. Dai, R. Qiao, R. Wang, J. Wu, Y. Liu, J. Peng, L. Chen, Y.-d. Chuang, F. Pan, Z.-x. Shen, G. Liu, H. Li, T. P. Devereaux, W. Yang, *Joule* **2021**, 5, 975.

[35] S. Lee, W. Jin, S. H. Kim, S. H. Joo, G. Nam, P. Oh, Y. K. Kim, S. K. Kwak, J. Cho, *Angew Chem Int Ed Engl* **2019**, 58, 10478.

[36] H. Yan, H. Wang, D. Wang, X. Li, Z. Gong, Y. Yang, *Nano Lett* **2019**, 19, 3280.

[37] Y. Zhu, X. He, Y. Mo, *Journal of Materials Chemistry A* **2016**, 4, 3253.